

**Electronic Supplemental Information (ESI):**

**In-Gap State Generated by La-on-Sr Substitutional Defects within the Bulk of SrTiO<sub>3</sub>**

Yoshihiro Aiura,<sup>\*a</sup> Kenichi Ozawa,<sup>b</sup> Yasuhisa Tezuka,<sup>c</sup> Makoto Minohara,<sup>a</sup> Akane Samizo,<sup>ad</sup> Kyoko Bando,<sup>e</sup> Hiroshi Kumigashira,<sup>fg</sup> Kazuhiko Mase,<sup>fh</sup>

<sup>a</sup> Electronics and Photonics Research Institute, National Institute of Advanced Industrial Science and Technology (AIST), Tsukuba, Ibaraki 305-8568, Japan

<sup>b</sup> Department of Chemistry, Tokyo Institute of Technology, Meguro, Tokyo 152-8551, Japan

<sup>c</sup> Graduate School of Science and Technology, Hirosaki University, Hirosaki, Aomori 036-8561, Japan

<sup>d</sup> Department of Materials Science and Technology, Faculty of Industrial Science and Technology, Tokyo University of Science, Katsushika, Tokyo 125-8585, Japan

<sup>e</sup> Nanomaterials Research Institute, National Institute of Advanced Industrial Science and Technology (AIST), Tsukuba, Ibaraki 305-8565, Japan

<sup>f</sup> Institute of Materials Structure Science, High Energy Accelerator Research Organization (KEK), Tsukuba, Ibaraki 305-0801, Japan

<sup>g</sup> Institute of Multidisciplinary Research for Advanced Materials, Tohoku University

<sup>h</sup> SOKENDAI (The Graduate University for Advanced Studies), Tsukuba, Ibaraki 305-0801, Japan

\*Corresponding Author: y.aiura@aist.go.jp

**S1. Rietveld analysis of SrTiO<sub>3</sub> and La<sub>0.05</sub>Sr<sub>0.95</sub>TiO<sub>3</sub>**

Commercially available pristine SrTiO<sub>3</sub> and La-doped SrTiO<sub>3</sub>, La<sub>0.05</sub>Sr<sub>0.95</sub>TiO<sub>3</sub>, single-crystals grown via the Verneuil method were used in the study (Crystal Base Co., Ltd.). For X-ray powder diffraction (XRD) measurement, the single-crystal samples were finely ground. Fig. S1 shows the XRD patterns of SrTiO<sub>3</sub> and La<sub>0.05</sub>Sr<sub>0.95</sub>TiO<sub>3</sub> measured by using the Bragg–Brentano configuration with CuK $\alpha$  radiation (PANalytical, X'Pert Pro MPD; 45 kV - 40 mA) at room temperature. The crystal structure of SrTiO<sub>3</sub> is cubic perovskite with a space group of  $Pm\bar{3}m$  (No. 221) at room temperature. When La is excessively substituted ( $x \geq 0.6$  for La<sub>x</sub>Sr<sub>1-x</sub>TiO<sub>3</sub>), it was reported that the crystal structure turns to be disordered perovskite.<sup>51,52</sup> However, in this study, the crystal structure at room temperature remains cubic perovskite without any distortion for low La-substituted SrTiO<sub>3</sub> (La<sub>0.05</sub>Sr<sub>0.95</sub>TiO<sub>3</sub>).<sup>53</sup> The XRD pattern of La<sub>0.05</sub>Sr<sub>0.95</sub>TiO<sub>3</sub> (Fig. S1) is essentially identical to that of SrTiO<sub>3</sub>, and does not exhibit peaks derived from any distortion of perovskite structure such as tetragonal ones. Assuming that the crystal structures of SrTiO<sub>3</sub> and La<sub>0.05</sub>Sr<sub>0.95</sub>TiO<sub>3</sub> correspond to cubic perovskites with a space group of  $Pm\bar{3}m$ , therefore, Rietveld analysis of the XRD patterns was performed by using the program RIETAN-FP.<sup>54</sup> From the Rietveld analysis, the lattice constants of SrTiO<sub>3</sub> and La<sub>0.05</sub>SrTiO<sub>3</sub> were estimated as 3.906 Å and 3.907 Å, respectively.

Extended X-ray absorption fine structure (XAFS) measurements were performed at low temperature (20 K). At the phase-transition temperature of 110 K, it is well known that the crystal structure of SrTiO<sub>3</sub> becomes to be distorted to tetragonal perovskite (*I4/mcm*) due to the rotation of the TiO<sub>6</sub> octahedral structure.<sup>55,56</sup> In the cubic structure without any distortion, there are 12 equivalent oxygen atoms adjacent to Sr. Given the rotation of the TiO<sub>6</sub> octahedron, the atomic distance to Sr decreases for four oxygen atoms and increases for the other four oxygen atoms. The remaining 4 oxygen atoms are barely affected by the rotation.

Hence, below the transition temperature, the Sr K-edge EXAFS peak in the primary coordination sphere caused by scattering from the nearest-neighbor 12 oxygen atoms should split into three peaks. However, it is difficult to detect a small splitting of the Sr-oxygen EXAFS peak since the rotation of the TiO<sub>6</sub> octahedron is slight (1.62° at 70 K).<sup>57</sup> Thus, in the curve fitting analysis of the EXAFS spectra, we assumed that the crystal structure corresponds

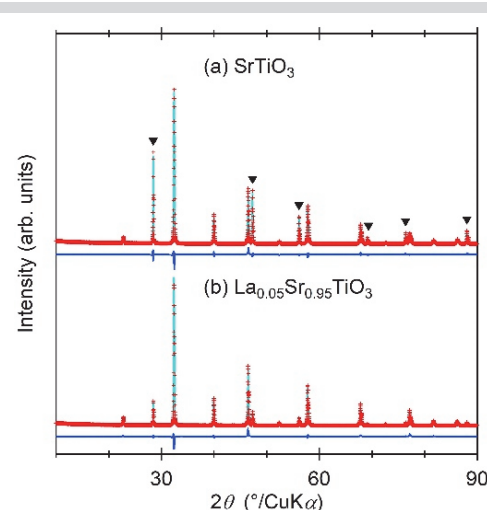


**Fig. S1** Observed XRD spectra (red), calculated XRD patterns (light-blue), and the differences (blue) of (a) SrTiO<sub>3</sub> and (b) La<sub>0.05</sub>Sr<sub>0.95</sub>TiO<sub>3</sub> resulting from Rietveld analysis. The diffraction angle of the observed XRD spectra is calibrated by using a Si internal standard (NIST 640e) denoted by ▼.

to cubic perovskite. Strictly speaking, the Sr-oxygen distance estimated by the curve fitting of EXAFS spectra is the average value of the three split distances.

It was reported that  $\text{La}_{0.05}\text{Sr}_{0.95}\text{TiO}_3$  also distorts below the transition temperature of 203 K.<sup>53</sup> A previous theoretical calculation indicated that carrier doping caused the cubic phase of the  $\text{TiO}_6$  octahedron to become electronically unstable and rotate.<sup>58</sup> However, as shown in the main text, the Sr K-edge EXAFS spectrum of  $\text{SrTiO}_3$  is extremely similar to that of  $\text{La}_{0.05}\text{Sr}_{0.95}\text{TiO}_3$ . Specifically, it is important to note that there is no significant change in the peak structure in the primary coordination sphere. This implies that the effect of local distortion on the oxygen atoms adjacent to Sr is not effective in  $\text{La}_{0.05}\text{Sr}_{0.95}\text{TiO}_3$  and is difficult to detect via EXAFS. Assuming that the crystal structures of  $\text{La}_{0.05}\text{Sr}_{0.95}\text{TiO}_3$  are cubic perovskites with the space group of  $Pm\bar{3}m$ , therefore, we performed the curve fitting analysis of EXAFS and compared it with the atomic distances estimated via the Rietveld analysis.

## S2. ARPES geometry and dipole selection rule

A schematic view of angle-resolved photoemission spectroscopy (ARPES) geometry in the study is shown in Fig. S2. The synchrotron radiation (SR) is linearly polarized horizontally and vertically to the detection plane, as denoted by LH-SR (yellow) and LV-SR (blue), respectively. The two orthogonal axes in the sample plane are denoted as  $x$  (horizontal) and  $y$  (vertical), and the surface normal is represented as  $z$ -axis. With respect to a high-resolution hemispherical electron analyzer (SES2002, Scienta) used in the study, photoelectrons in the acceptance angle of  $\pm 6^\circ$ , which is denoted by the ‘detection area’ (red), can be simultaneously taken for the angular mode. The entrance slit of the electron analyzer lies on the incidence plane of SR. The polar ( $\vartheta$ ) and tilt ( $\phi$ ) angles denote the rotation around the  $y$ -axis and  $x$ -axis with respect to the lens axis of the analyzer ( $\vartheta=0^\circ$ ) and the detection plane ( $\varphi=0^\circ$ ), respectively. The polar-rotational and tilt-rotational control of the sample are obtained via a rotary stage and a sample goniometer with a liquid-helium-flow cryostat (*i*-GONIO LT, R-Dec Co. Ltd.),<sup>59</sup> respectively. Fig. S2 shows the ARPES geometry when the surface normal lies on the detection plane, i.e., the tilt angle is set to  $0^\circ$ .

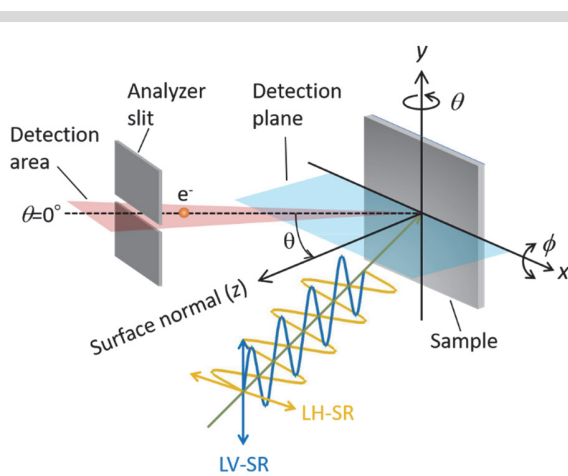


**Fig. S2** Schematic view of the ARPES geometry.

In our ARPES measurements, the (001) surfaces of  $\text{SrTiO}_3$  and  $\text{La}_{0.05}\text{Sr}_{0.95}\text{TiO}_3$  were used, and the [100] and [010] directions of the samples were aligned with the  $x$ -axis and  $y$ -axis, respectively. By doping electrons into  $\text{SrTiO}_3$ , it is considered that the  $\text{Ti} 3d t_{2g}$  bands near the conduction band minimum around the  $\Gamma$  point are partially occupied.<sup>510,511</sup> In the bulk, the  $t_{2g}$  bands consisting of the  $d_{xy}$ ,  $d_{yz}$ , and  $d_{zx}$  orbitals degenerate at the  $\Gamma$  point.<sup>510</sup> Conversely, near the surface, the  $t_{2g}$  bands split into the in-plane  $d_{xy}$  band and the out-of-plane  $d_{yz}/d_{zx}$  bands due to the discontinuous potential at the (001) surface. In a recent high-resolution ARPES study, which is a surface-sensitive spectroscopic technique, the aforementioned splitting of the  $t_{2g}$  bands around the  $\Gamma$  point was clearly observed.<sup>511</sup>

Based on Fermi’s golden rule, the photoemission intensity is only detected when the entire matrix element  $\langle \varphi_f^k | \mathbf{A} \cdot \mathbf{p} | \varphi_i^k \rangle$  is symmetric (or even) with respect to the symmetry operation to the mirror plane of the crystal.<sup>512,513</sup> Here,  $|\varphi_i^k\rangle$  and  $|\varphi_f^k\rangle$  denote the initial and final states, respectively. Additionally,  $\mathbf{A}$  and  $\mathbf{p}$  denote a vector potential of the electromagnetic field and a momentum operator. A vacuum ultraviolet photon energy around 100 eV is used in the ARPES study, and thus, the photoelectrons behave in a free-electron-like manner and the final state  $|\varphi_f^k\rangle$  is symmetric (even) with respect to the mirror plane. In order to detect the photoelectrons, the initial state  $|\varphi_i^k\rangle$  and dipole operator  $\mathbf{A} \cdot \mathbf{p}$  must exhibit the same symmetry with respect to the mirror plane. In the ARPES geometry shown in Fig. S2, the LH-SR and LV-SR exhibit symmetry (even) and asymmetry (odd) with respect to the detection plane (i.e.,  $zx$ -mirror plane detection plane), respectively. With respect to the initial state, the  $d_{zx}$  band is symmetric (even) while the  $d_{xy}$  and  $d_{yz}$  bands are asymmetric (odd). Given the restriction of the dipole selection rule, the detectable initial states for the geometry in this ARPES study are summarized as follows:

$d_{zx}$  band (even) for LH-SR (even),  
 $d_{xy}$  and  $d_{yz}$  bands (odd) for LV-SR (odd).

## S3. Photoemission spectroscopy of $\text{La}_{0.05}\text{Sr}_{0.95}\text{TiO}_3$

Commercially available La-doped  $\text{SrTiO}_3$ ,  $\text{La}_{0.05}\text{Sr}_{0.95}\text{TiO}_3$ , single-crystals grown via the Verneuil method (Crystal Base Co., Ltd.) were used in the photoemission spectroscopy (PES) study. In order to prevent the composition from deviating from the bulk value, clean surfaces were obtained via cleaving the single crystal *in situ* at a temperature of 20 K. The surface normal and the measured momentum direction were set such that they constitute a naturally cleaving (001) surface and [100] direction, respectively. All PES and angle-resolved PES (ARPES) measurements were performed at 20 K.

Fig. S3 shows the valence band spectra of the  $\text{La}_{0.05}\text{Sr}_{0.95}\text{TiO}_3$  (001) surface obtained at (a)  $\vartheta=0^\circ$  and (b)  $\vartheta=18^\circ$ . The spectra were measured by using LH-SR (black) and LV-SR (red), respectively, of 100 eV. The spectra obtained at  $\vartheta=0^\circ$  and  $18^\circ$  reflect the electronic structure of valence bands around the center of the first and second Brillouin zones (BZs), respectively. In our experimental condition, the characteristic spectral feature immediately below the Fermi level ( $E_F$ ) denoted as the metallic state (MS) was clearly observed around the center of the second BZ ( $\Gamma_2$ ) only for the LV-SR (red curve in Fig. S3 (b)). As mentioned in section 2, the MS is considered as derived from electron doping into the  $d_{xy}$  and  $d_{yz}$  bands. Interestingly, the characteristic spectral feature was not observed

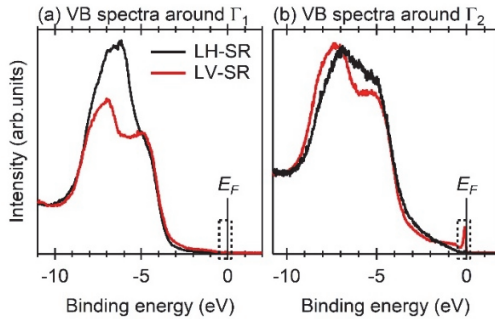


**Fig. S3** Polarization dependence of the valence band spectra of the  $\text{La}_{0.05}\text{Sr}_{0.95}\text{TiO}_3$  (001) surface around (a)  $\Gamma_1$  and (b)  $\Gamma_2$ . The spectra denoted by the black and red lines are measured by using LH-SR and LV-SR, respectively. The photon energy was set to be 100 eV. The spectra were measured at 20 K.

in the spectrum around the center of the first BZ ( $\Gamma_1$ ). We speculate that the lack of spectral intensity around  $\Gamma_1$  is due to the final-state-effect as typically observed for other metal oxides.<sup>S14</sup> Although there is a possibility of detecting the trace of the  $d_{zx}$  band in the case that LH-SR is used, no spectral intensity was observed immediately below  $E_F$  in the observed PES spectra.

In order to demonstrate the electronic behavior of the  $t_{2g}$  bands more clearly, the ARPES images in the energy region as indicated by the dotted rectangles in Fig. S3 were measured. Fig. S4 (a) shows the spectra at  $\vartheta=0^\circ$ ,  $8^\circ$ , and  $18^\circ$  as measured by using LV-SR. A characteristic electronic structure with parabolic shape, which recently attracted attention as a two-dimensional electron

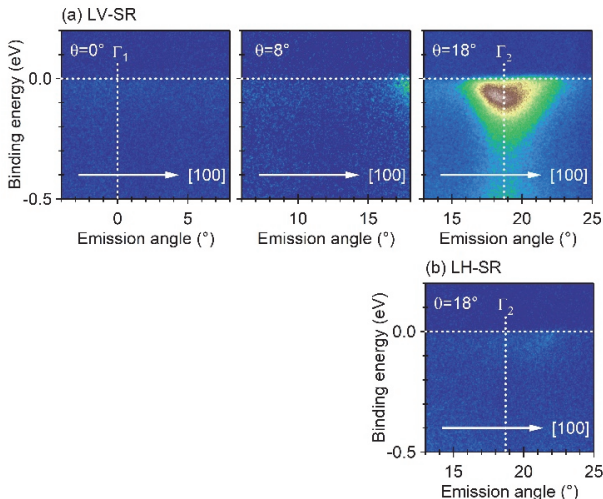
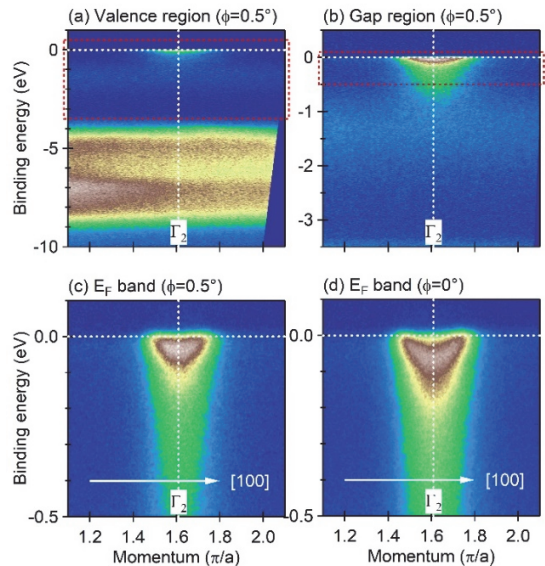


**Fig. S4** Polar angle dependence of the ARPES images of the  $\text{La}_{0.05}\text{Sr}_{0.95}\text{TiO}_3$  (001) surface near  $E_F$ . The images are measured by using LV-SR, and normalized by the integrated intensity of valence bands. (b) ARPES image images near  $E_F$  measured by using LH-SR. The polar angle is the same as that used in the upper-right image measured by using LV-SR. The photon energy was set to be 100 eV.

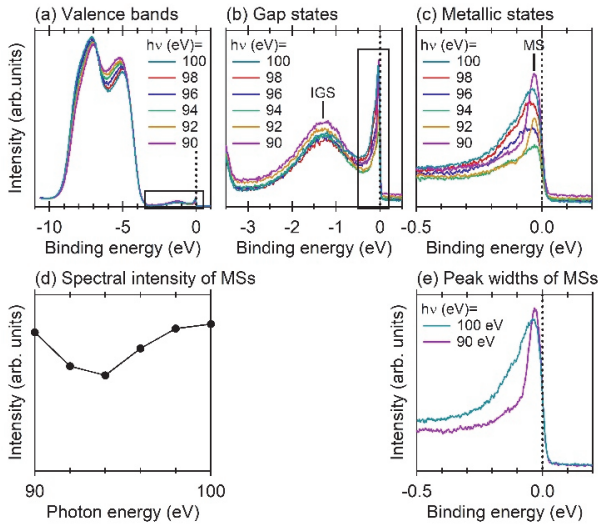
gas (2DEG),<sup>S11, S15-S19</sup> was observed only around  $\Gamma_2$ . The parabolic spectral feature immediately below  $E_F$  was not observed in the ARPES image measured via LH-SR (Fig. S4 (b)).

Fig. S5 (a) shows the ARPES image in the valence band of the  $\text{La}_{0.05}\text{Sr}_{0.95}\text{TiO}_3$  (001) surface. As indicated in previous reports, it is well known that two remarkable structures centered at the binding energy of approximately -5 eV and approximately -7.5 eV are derived from O  $2p$  non-bonding bands and Ti  $3d$ -O  $2p$  bonding bands, respectively.<sup>S10</sup> In addition to the valence bands characteristic of the pristine (non-doped)  $\text{SrTiO}_3$ , electron doping due to the  $\text{La}^{3+}$ -on- $\text{Sr}^{2+}$  substitution induces two characteristic states in the band gap region. Fig. S5 (b) shows the expanded ARPES image in the band gap region indicated by the red rectangle in Fig. S5 (a). The ARPES image was measured by using LV-SR, and thus, the partially occupied  $d_{xy}$  and/or  $d_{yz}$  bands were observed only around  $\Gamma_2$ . As shown in Figs. S5 (c) and S5 (d), i.e., the expanded views near  $E_F$  in the energy region indicated by the red rectangle in Fig. S5 (b), the  $d_{xy}/d_{yz}$  bands immediately below  $E_F$  are considerably dispersive and sensitive to the tilt angle. In addition to the dispersive  $d_{xy}/d_{yz}$  bands, a non-dispersive state at the binding energy of -1.3 eV was observed throughout the measured momentum region. The non-dispersive state is always located within the band gap, and thus, it is hereafter referred to as an in-gap state (IGS).

Fig. S6 shows the photon energy ( $h\nu$ ) dependence of the PES spectra from 90 eV to 100 eV. The PES spectra were measured in the transmission mode. In order to clarify the photon energy dependence of the  $d_{xy}/d_{yz}$  bands, the LV-SR was used and the polar angle was set such that the momentum at  $E_F$  is around  $\Gamma_2$  ( $\vartheta=18^\circ$ ). As shown in the PES spectra near  $E_F$  (Fig. S6 (c)), the spectral shape



**Fig. S5** ARPES images in (a) valence-band region, (b) band-gap region, and (c) near Fermi-level region of  $\text{La}_{0.05}\text{Sr}_{0.95}\text{TiO}_3$  (001) around  $\Gamma_2$ . The spectra are measured by using LV-SR. For the ARPES images in the panels (a), (b), and (c), the sample normal is inclined  $0.5^\circ$  from the detection plane, i.e., the tilt angle ( $\phi$ ) is set to  $0.5^\circ$ . (d) The same as panel (c), but the sample normal is set to the detection plane ( $\phi=0^\circ$ ). The photon energy was set to be 100 eV.



**Fig. S6** (a) Photon energy dependence of the valence bands around  $\Gamma_2$ . (b) and (c) Expanded views in the binding-energy region denoted by the rectangles in the panels (a) and (b), respectively. (d) Spectral intensity integration of the binding energy region from -0.5 eV to 0.2 eV. (e) Comparison of the peak widths in the vicinity of  $E_F$  measured at the photon energy of 100 eV (green) and 90 eV (violet). The spectra are measured by using LV-SR, and normalized by the integrated intensity of valence bands.

of the  $d_{xy}/d_{yz}$  bands strongly depends on the photon energy. The spectral width of the  $d_{xy}/d_{yz}$  bands at  $h\nu=90$  eV is considerably sharp when compared with that at  $h\nu=100$  eV (Fig. S6 (e)). The spectral intensity of  $d_{xy}/d_{yz}$  bands gradually decreases as the photon energy decreases from 100 eV to 94 eV, and turns to increase as the photon energy further decreases (Fig. S6 (d)). As shown in the following ARPES images (Fig. 2 in the main text), this suggests that the MS is caused by multiple states with different photon energy dependence in the spectral intensity. Conversely, the IGSs did not indicate any remarkable  $h\nu$ -dependence.

Fig. S7 (b) shows the tilt ( $\phi$ ) dependence of the PES spectra in the band-gap region around  $\Gamma_2$ . The spectra were measured by using LV-SR and normalized by the integrated intensity of the valence bands as shown in Fig. S7 (a). A photon energy of 100 eV was used. The tilt angle was changed from -3.0° to +3.0° in steps of 0.5°. The black bold lines indicate the PES spectra measured when the surface normal was set in the detection plane, i.e.,  $\phi=0^\circ$ . As shown in Fig. S7 (b), the spectral shape/intensity of the IGS barely depends on the tilt angle. Conversely, the spectral intensity near  $E_F$  is the most intensive at  $\phi=0^\circ$ , and monotonically decreases as the tilt angle increases/decreases. As mentioned above, the sharp MS at  $\phi=0^\circ$  is considered as derived from the  $d_{xy}$  band. It should be noted that the MS is clearly observed even when  $\phi=\pm 3.0^\circ$ . The  $d_{xy}$  and  $d_{yz}$  bands must be detected only near  $\phi=0^\circ$ . The MS observed when  $\phi=\pm 3.0^\circ$  is potentially caused by the  $d_{zx}$  band due to its less-dispersive nature along the  $y$ -axis. From the dipole selection rules as discussed in the section 2, the  $d_{zx}$  band should not be detected when the surface normal lies on the detection plane ( $\phi=0^\circ$ ). However, the PES intensity no longer follows the dipole selection rule when the sample is tilted. Furthermore, the  $t_{2g}$  bands are consid-

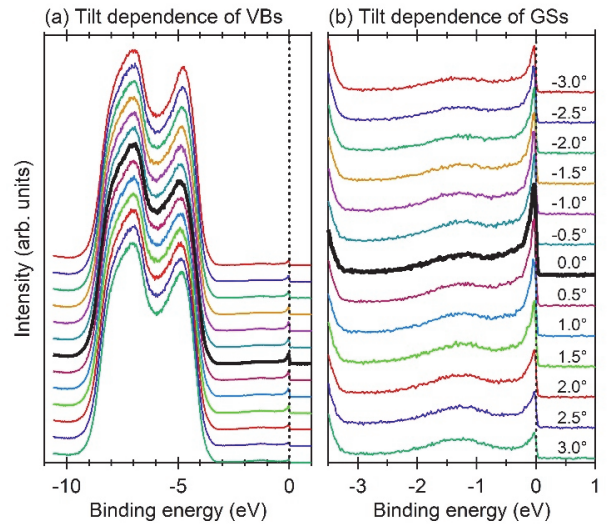


**Fig. S7** Tilt dependence of PES spectra in (a) valence-band region and (b) band gap region around  $\Gamma_2$ . The spectra are obtained by using LV-SR and normalized by the integrated intensity of the valence band spectra.

ered to be hybridized to each other with the exception of  $\Gamma$ . Therefore, we consider that the MS observed at the finite tilt angle is caused by the deviation from the dipole selection rule and/or the hybridization among the  $t_{2g}$  bands. The origin of the spectral feature near  $E_F$  has been actively discussed in recent years.<sup>S16-S19</sup>

#### S4. Soft X-ray emission spectroscopy of SrTiO<sub>3</sub> and La<sub>0.05</sub>Sr<sub>0.95</sub>TiO<sub>3</sub>

Commercially available pristine SrTiO<sub>3</sub> and La-doped SrTiO<sub>3</sub>, La<sub>0.05</sub>Sr<sub>0.95</sub>TiO<sub>3</sub>, single-crystals grown via the Verneuil method (Crystal Base Co., Ltd.) were used in the soft X-ray emission spectroscopy (SXES) study. The surface normal and the horizontal direction were set as the naturally cleaving (001) surface and the [100] direction, respectively. All SXES spectra were measured at room temperature. The XRD spectra in Fig. S1 show that La-doped SrTiO<sub>3</sub> at the doping level (5 at%) has a non-distorted cubic perovskite structure like that of pristine SrTiO<sub>3</sub>. In the symmetrical crystal field of cubic perovskite without any distortion, the Ti 3d state splits into threefold-degenerated  $t_{2g}$  and twofold-degenerated  $e_g$  states.

The SXES measurements were performed at the BL-16 undulator beamline at the Photon Factory (PF), KEK. A soft X-ray spectrometer based on the Rowland circle geometry that incorporates a spherical grating and a multi photo-counting detector was used.<sup>S20</sup> The scattered photons were detected in the horizontal plane, and the SXES spectra were acquired at a 90° scattering angle from the incident SR. The SR was linearly polarized horizontally and vertically to the detection plane. The SXES measurement arrangements using the horizontally and vertically linear-polarized SR are denoted as depolarized and polarized configurations, respectively.<sup>S20</sup> The SXES spectra were measured at room temperature and normalized by the SR intensity. The full width at half maximum of the elastic peak in the SXES spectra of pristine SrTiO<sub>3</sub> was estimated as 0.48 eV. In order to calibrate the energy scale of the spectrometer, X-ray absorption spectra (XAS) acquired in the total

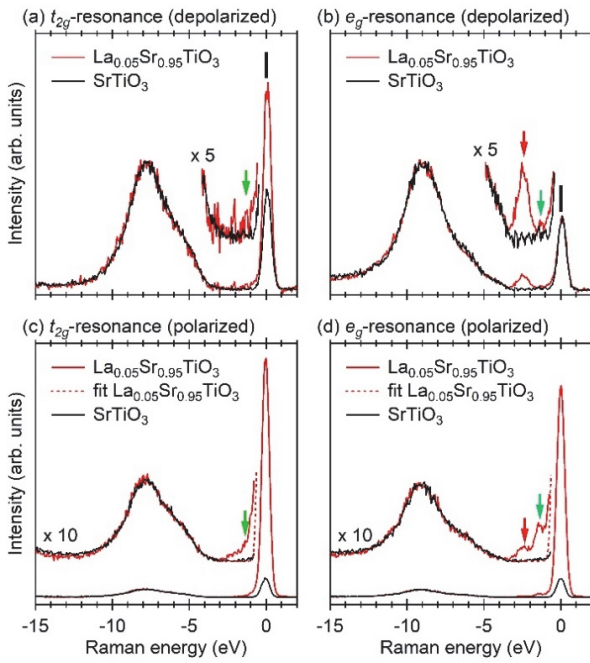


**Fig. S8** Polarization dependence of Ti 2p-resonance SXES spectra of  $\text{La}_{0.05}\text{Sr}_{0.95}\text{TiO}_3$  (red) and  $\text{SrTiO}_3$  (black). (a) and (b)  $t_{2g}$ -resonance and  $e_g$ -resonance SXES spectra, respectively, measured at the depolarized configuration. (c) and (d)  $t_{2g}$ -resonance and  $e_g$ -resonance SXES spectra, respectively, measured at the polarized configuration. In order to show the faint spectral feature near the elastic peak clearly, the expanded spectra are also observed. With respect to the spectra measured at the polarized configuration, the elastic peaks are fitted by using Gaussian function. The dotted lines in the panels (c) and (d) show the tail of the best-fitted Gaussian function. The spectra are normalized by the integrated intensity from -4 eV to -12 eV.

electron yield (TEY) mode were measured at the BL-13B undulator beamline at PF, KEK<sup>S21</sup> and were compared with XAS spectra measured at BL-16. High-resolution PES was performed at the BL-13B beamline, and thus, it was possible to estimate the accurate photon energy from the energy difference between the PES spectra by the primary SR and the PES spectra by the secondary SR.

As discussed in the main text, it is considered that the characteristic spectral change in the SXES spectra measured at the depolarized configuration (Fig. 4(c)) was caused by the d-d transition from the itinerant  $t_{2g}$  bands occupied by La doping. In order to determine the vestige of the excitation of IGS in the SXES spectra, we measured the SXES spectra at the polarized configuration and compared them with those at the depolarized configuration. Fig. S8 shows the polarization dependence of Ti 2p-resonance SXES spectra. Panels (a) and (b) denote the SXES spectra measured at the depolarized configuration excited at photon energy corresponding to the  $L_{\text{III}} \rightarrow t_{2g}$  absorption ( $t_{2g}$ -resonance SXES) and  $L_{\text{III}} \rightarrow e_g$  absorption ( $e_g$ -resonance SXES), respectively. The corresponding  $t_{2g}$ -resonance and  $e_g$ -resonance SXES spectra measured at the polarized configuration are shown in Figs. S8 (c) and S8 (d),

respectively. In the SXES spectra measured at the polarized configuration, the elastic peaks are significantly intense for the La-doped  $\text{SrTiO}_3$  (red), but not for the pristine  $\text{SrTiO}_3$  (black). This tendency is similar to previous results on the polarization dependence of  $\text{TiO}_2$  and  $\text{Ti}_2\text{O}_3$ .<sup>S22, S23</sup> In  $\text{Ti} 2p$  SXES spectra measured at the polarized configuration, the elastic peak of  $\text{TiO}_2$  with the formal  $d^0$  configuration was significantly weaker than that of  $\text{Ti}_2\text{O}_3$  with the formal  $d^1$  configuration. We conjecture that the elastic peak significantly increases in the SXES spectra measured at the polarized configuration by doping electrons into the Ti oxides without  $d$  electrons such as  $\text{TiO}_2$  and  $\text{SrTiO}_3$ .

In addition to the elastic peak, it must be noted that, in the  $e_g$ -resonance SXES spectrum measured at the polarized configuration (Fig. S8 (d)), the two characteristic peaks denoted by the red and green arrows, are induced by La doping. The peak structure denoted by the red arrow is located at -2.3 eV away from the elastic-scattering peak. The observed energy shift (-2.3 eV) was identical to that of the peak due to the inelastic scattering in the SXES spectrum measured at the depolarized configuration (Fig. S8 (b)), and thus, it is considered that the origin is the  $d$ - $d$  transition from the occupied itinerant  $t_{2g}$  state to the unoccupied  $e_g$  bands. In addition to the inelastic peak at -2.3 eV, it is observed that another peak structure exists near the elastic-scattering peak as denoted by the green arrow in Fig. S8 (d). In the SXES spectra of  $\text{LaAlO}_3/\text{SrTiO}_3$  heterostructure, a fluorescence spectral feature was observed near the elastic-scattering peak.<sup>S19, S24, S25</sup> In the  $e_g$ -resonance SXES spectrum, however, the fluorescence peak should overlap with the inelastic peak at -2.3 eV. The observed energy position of -1.3 eV was almost identical to that of the inelastic peak due to the  $d$ - $d$  transition from the occupied IGS to the unoccupied  $t_{2g}$  bands as reported previously.<sup>S26-S28</sup> In our  $t_{2g}$ -resonance SXES spectra also (Figs. S8 (a) and S8 (c)), it was shown that the spectral intensity near the tail structure of elastic-scattering increases via La doping. However, the reported inelastic peak due to IGS- $t_{2g}$  transition was observed in the  $t_{2g}$ -resonance SXES spectra, but not in the  $e_g$ -resonance SXES spectra.

Finally, we discuss the origin of peak at -1.3 eV observed in the  $e_g$ -resonance SXES spectra. Prior to this, we briefly summarize the origin of inelastic scatterings observed in the SXES spectra by using schematic diagrams. Fig. S9 shows possible  $d$ - $d$  transitions in the SXES spectra. In the  $t_{2g}$ -resonance SXES spectra (Fig. S9 (a)), it is considered that the inelastic (or Raman) scatterings are derived from  $d$ - $d$  transitions from the itinerant/localized (occupied)  $t_{2g}$  bands occurred denoted by MS/IGS to the unoccupied  $t_{2g}$  bands. The MS- $t_{2g}$  Raman scattering (Final #1 in Fig. S9 (a)) was observed as the increase in the spectral intensity of the zero-loss peak by La doping observed in the SXES spectra measured at the depolarized configuration (Fig. S8 (a)). The IGS- $t_{2g}$  Raman scattering (Final #2) was observed as the increase in the spectral intensity near the tail structure of elastic peak by La doping observed in the  $t_{2g}$ -resonance SXES spectra (Figs. S8 (a) and S8 (c)). With respect to the normal  $e_g$ -resonance Raman scattering also (Fig. S9 (b)), the inelastic scatterings derived from  $d$ - $d$  transitions from the occupied MS/IGS are expected. It is well known that the MS- $e_g$  Raman scattering (Final #3 in Fig. S9 (b)) appears as the inelastic peak around -2.3 eV in the  $e_g$ -resonance SXES spectra as previously reported.<sup>S24-S26, S29</sup> As shown in Final #3 of Fig. S9 (b), it is considered that the Raman shift (-2.3 eV) represents a magnitude that slightly exceeds the crystal-field splitting (10Dq). The Raman shift due to IGS- $e_g$

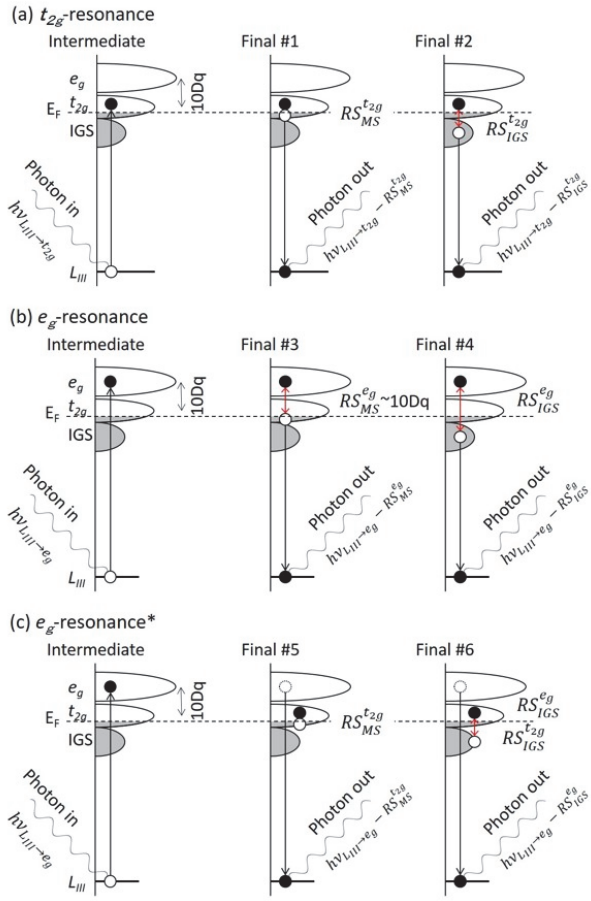


**Fig. S9** Schematic diagrams of possible  $d$ - $d$  transitions in (a) the  $t_{2g}$  resonance and (b) the  $e_g$ -resonance SXES spectra. (c) Conceptual inelastic processes derived from the excitation from the metallic (itinerant) state/IGS to the  $t_{2g}$  band when the excited  $e_g$  electrons relax to the original  $L_{III}$  state.

transition (Final #4) is expected to correspond to the energy difference between the energy of occupied IGS and that of unoccupied  $e_g$  bands (approximately -3.7 eV), but has not observed to date.

As mentioned above, the peak at -1.3 eV observed in the  $e_g$ -resonance spectra (Fig. S8 (d)) was not due to the fluorescence previously reported.<sup>S24, S25</sup> Furthermore, it cannot explain the origin of peak at -1.3 eV by the normal  $e_g$ -resonance process shown in Fig. S9 (b). Although the reason for the abnormal increase in the intensity of the elastic peak as observed in the  $e_g$ -resonance SXES spectra measured at the polarized configuration (Figs. S8 (c) and S8 (d)) is not clear, we speculate that the occupied IGS has transitioned to the unoccupied  $t_{2g}$  bands by the intense radiation emitted when the excited  $e_g$  electrons relax to the  $L_{III}$  state (Final #6). The inelastic peak is expected to appear at the same energy position as Final #2 in Fig. S9 (a). Actually, the observed peak position in the  $e_g$ -resonance SXES spectra measured at the polarized configuration (Fig. S8 (d)) was almost the same as that in the  $t_{2g}$ -resonance SXES spectra in the depolarized configuration (Fig. S8 (b)). However, a detailed measurement on the SR-

energy dependence around the  $e_g$ -resonance energy is desirable to provide clear evidence that the peak at -1.3 eV is derived from the inelastic peak. If the IGS- $t_{2g}$  transition occurs in the relaxation process, the excitation from the occupied MS to the unoccupied  $t_{2g}$  bands (Final #5) should also simultaneously occur. However, in the SXES spectra measured at the polarized configuration, it is considered to be difficult to detect inelastic peak due to the MS- $t_{2g}$  transition because of the intense elastic peak by La doping.

### S5. X-ray absorption fine structure of SrTiO<sub>3</sub> and La<sub>0.05</sub>Sr<sub>0.95</sub>TiO<sub>3</sub>

Commercially available pristine SrTiO<sub>3</sub> and La-doped SrTiO<sub>3</sub>, La<sub>0.05</sub>Sr<sub>0.95</sub>TiO<sub>3</sub>, single-crystals grown via the Verneuil method (Crystal Base Co., Ltd.) are used in X-ray absorption fine structure (XAFS) study. In order to acquire the XAFS spectra in the transmission mode, the single-crystal samples are finely ground, mixed with boron nitride powder, and subsequently pressed to form discs with a diameter of approximately 8 mm and a thickness of approximately 1 mm. The Sr K/La K-edge XAFS measurements are performed at the beamline AR-NW10A of the Photon Factory Advanced Ring (PF-AR), KEK.<sup>S30, S31</sup> In order to estimate the local structure around the Sr/La atoms in detail, the spectra are measured at 20 K. The data processing of the extended XAFS (EXAFS)

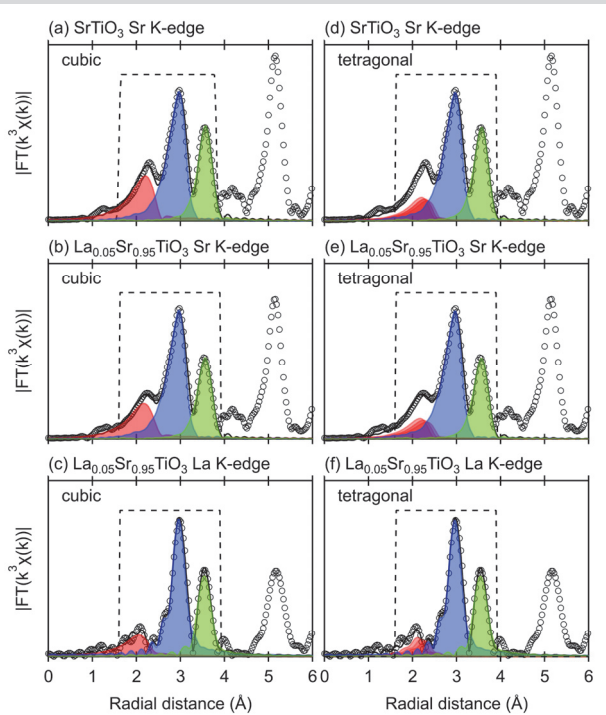


**Fig. S10** Best fitted curves (black lines) to  $k^3$ -weighted Fourier transformed spectra (open circles) of (a)/(d) Sr K-edge EXAFS of SrTiO<sub>3</sub>, (b)/(e) Sr K-edge EXAFS of La<sub>0.05</sub>Sr<sub>0.95</sub>TiO<sub>3</sub>, and (c)/(f) La K-edge EXAFS of La<sub>0.05</sub>Sr<sub>0.95</sub>TiO<sub>3</sub>. The curve fittings are performed in the first three single-scattering regions denoted by the dotted lines. The contributions of Sr-O, Sr-Ti, and Sr-Sr single scatterings are also indicated by red, blue, and green lines, respectively. Panels (a)-(c) and (d)-(f) show the curve fitting results for the undistorted cubic perovskite structure ( $Pm\bar{3}m$ ) and distorted tetragonal perovskite structure ( $I4/mcm$ ), respectively.

spectra is performed by using Athena and curve fitting by using Artemis.<sup>S32</sup>

As shown in Fig. 6 of the main text, atomic distance between Sr and the nearest-neighbor O atoms ( $d_{Sr-O}$ ) is differs from that between La and the nearest-neighbor O atoms ( $d_{La-O}$ ). In order to quantitatively estimate the atomic distance between Sr/La atoms and the neighboring atoms, we perform the curve fit analysis to the empirical Fourier transformed spectra.<sup>S32</sup> Fig. S10 shows the best fitted curves fitting in the first three single-scattering region as denoted by the dotted lines. The open circles denote the empirical Fourier transform of the  $k^3$ -weighted EXAFS spectra, and the red, blue, and green lines denote the contribution from Sr-O, Sr-Ti, and Sr-Sr single-scattering paths, respectively. The curve fitting is performed by assuming that the crystal structure corresponds to cubic perovskite ((a)-(c)) or tetragonal perovskite ((d)-(f)). As shown in the figures, the crystal distortion only merely causes a slight splitting of the first peak caused by the nearest-neighbor O atoms around Sr. Giving the spatial resolution of the EXFAS spectra, splitting width estimated via curve fitting is meaningless. Thus, in the main text, the crystal structure is discussed as a cubic structure. Strictly speaking, the estimated atomic distances between Sr and the nearest-neighbor oxygens indicate the average value of atomic distances for the distorted perovskite structure.

## References

- S1 Y. Fujishima, Y. Tokura, T. Arima and S. Uchida, *Phys. Rev. B* 1992, **46**, 11167-11170.
- S2 Y. Tokura, Y. Taguchi, Y. Okada, Y. Fujishima, T. Arima, K. Kumagai and Y. Iye, *Phys. Rev. Lett.* 1993, **70**, 2126-2129.
- S3 T. Ozaki, Y. K. Kusunose, H. Yamaguchi, K. Kajiwara and Y. Chikaura, *Phase Trans.* 2011, **84**, 837-842.
- S4 F. Izumi and K. Momma, *Solid State Phenom.* 2007, **130**, 15-20.
- S5 F. W. Lytle, *J. Appl. Phys.* 1964, **35**, 2212-2215.
- S6 G. Shirane and Y. Yamada, *Phys. Rev.* 1969, **177**, 858-863.
- S7 T. Ikeda, T. Kobayashi, M. Takata, T. Takayama and M. Sakata, *Solid State Ion.* 1998, **108**, 151-157.
- S8 K. Uchida and S. Tsuneyuki, *Phys. Rev. B* 2003, **68**, 174107.
- S9 Y. Aiura, H. Bando, T. Miyamoto, A. Chiba, R. Kitagawa, S. Maruyama and Y. Nishihara, *Rev. Sci. Instrum.* 2003, **74**, 3177-3179.
- S10 Y. Aiura, I. Hase, H. Bando, T. Yasue, T. Saitoh and D. S. Dessau, *Surf. Sci.* 2002, **515**, 61-74.
- S11 N. C. Plumb, M. Salluzzo, E. Razzoli, M. Månnsson, M. Falub, J. Krempasky, C. E. Matt, J. Chang, M. Schulte, J. Braun, H. Ebert, J. Minář, B. Delley, K.-J. Zhou, T. Schmitt, M. Shi, J. Mesot, L. Patthey and M. Radović *Phys. Rev. Lett.* 2014, **113**, 086801.
- S12 S. Hüfner, *Photoelectron Spectroscopy*; Springer-Verlag: Berlin, Heidelberg, 1995.
- S13 H. Iwasawa, K. Shimada, E. F. Schwier, M. Zheng, Y. Kojima, H. Hayashi, J. Jiang, M. Higashiguchi, Y. Aiura, H. Namatame and M. Taniguchi, *J. Synchrotron Rad.* 2017, **24**, 836-841.
- S14 Y. Aiura, K. Ozawa, E. F. Schwier, K. Shimada and K. Mase, *J. Phys. Chem. C* 2018, **122**, 19661-19669.
- S15 A. F. Santander-Syro, C. Bareille, F. Fortuna, O. Copie, M. Gabay, F. Bertran, A. Taleb-Ibrahimi, P. Le Fèvre, G. Herranz, N. Reyren, M. Bibes, A. Barthélémy, P. Lecoer, J. Guevara and M. J. Rozenberg, *Phys. Rev. B* 2012, **86**, 121107(R).
- S16 P. D. C. King, S. McKeown Walker, A. Tamai, A. de la Torre, T. Eknaphakul, P. Buaphet, S.-K. Mo, W. Meevasana, M. S. Bahramy and F. Baumberger, *Nat. Commun.* 2014, **5**, 3414.
- S17 T. C. Rödel, C. Bareille, F. Fortuna, C. Baumier, F. Bertran, P. Le Fèvre, M. Gabay, O. Hijano Cubelos, M. J. Rozenberg, T. Maroutian, P. Lecoer and A. F. Santander-Syro, *Phys. Rev. Appl.* 2014, **1**, 051002.
- S18 A. F. Santander-Syro, F. Fortuna, C. Bareille, T. C. Rödel, G. Landolt, N. C. Plumb, J. H. Dil and M. Radović, *Nat. Mater.* 2014, **13**, 1085-1090.
- S19 N. C. Plumb, M. Kobayashi, M. Salluzzo, E. Razzoli, C. E. Matt, V. N. Strocov, K. J. Zhou, M. Shi, J. Mesot, T. Schmitt, L. Patthey and M. Radović, *Appl. Surf. Sci.* 2017, **412**, 271-278.
- S20 Y. Harada, H. Ishii, M. Fujisawa, Y. Tezuka, S. Shin, M. Watanabe, Y. Kitajima and A. Yagishita, *J. Synchrotron Rad.* 1998, **5**, 1013-1015.
- S21 A. Toyoshima, T. Kikuchi, H. Tanaka, K. Mase, K. Amemiya and K. Ozawa, *J. Phys.: Conf. Ser.* 2013, **425**, 152019.
- S22 Y. Tezuka, N. Nakajima, J. Adachi, O. Morimoto, H. Sato and T. Uozumi, *J. Phys. Soc. Jpn.* 2017, **86**, 124713.
- S23 Y. Tezuka, N. Nakajima and O. Morimoto, *J. Electron Spectrosc. Relat. Phenom.* 2011, **184**, 216-219.
- S24 K. J. Zhou, M. Radovic, J. Schlappa, V. Strocov, R. Frison, J. Mesot, L. Patthey and T. Schmitt, *Phys. Rev. B* 2011, **83**, 201402(R).
- S25 F. Pfaff, H. Fujiwara, G. Berner, A. Yamasaki, H. Niwa, H. Kiuchi, A. Gloskovskii, W. Drube, J. Gabel, O. Kirilmaz, A. Sekiyama, J. Miyawaki, Y. Harada, S. Suga, M. Sing and R. Claessen, *Phys. Rev. B* 2018, **97**, 035110.
- S26 T. Higuchi, T. Tsukamoto, M. Watanabe, M. M. Grush, T. A. Callcott, R. C. Perera, D. L. Ederer, Y. Tokura, Y. Harada, Y. Tezuka and S. Shin, *Phys. Rev. B* 1999, **60**, 7711-7714.
- S27 T. Higuchi, T. Tsukamoto, M. Watanabe, Y. Harada, Y. Tezuka, Y. Tokura and S. Shin, *Physica B* 2000, **281&282**, 615-616.
- S28 T. Higuchi, T. Takeuchi, T. Tsukamoto, Y. Harada, Y. Taguchi, Y. Tokura and S. Shin, *Nucl. Instrum. Methods Phys. Res. B* 2003, **199**, 386-390.
- S29 T. Higuchi, D. Baba, T. Takeuchi, T. Tsukamoto, Y. Taguchi, Y. Tokura, A. Chainani and S. Shin, *Phys. Rev. B* 2003, **68**, 104420.
- S30 M. Nomura, Y. Koike, M. Sato, A. Koyama, Y. Inada and K. Asakura, *AIP Conf. Proc.* 2006, **882**, 896-898.
- S31 Y. Aiura, K. Ozawa, I. Hase, H. Bando, H. Haga, H. Kawanaka, A. Samizo, N. Kikuchi and K. Mase, *J. Phys. Chem. C* 2017, **121**, 9480-9488.
- S32 B. Ravel and M. Newville, *J. Synchrotron Radiat.* 2005, **12**, 537-541.